

Grain Boundary Complexions Enable a Simultaneous Optimization of Electron and Phonon Transport Leading to High-Performance GeTe Thermoelectric Devices

Chaohua Zhang,* Gan Yan, Yibo Wang, Xuelian Wu, Lipeng Hu, Fusheng Liu, Weiqin Ao, Oana Cojocaru-Mirédin, Matthias Wuttig, G. Jeffrey Snyder, and Yuan Yu*

Grain boundaries (GBs) form ubiquitous microstructures in polycrystalline materials which play a significant role in tuning the thermoelectric figure of merit (ZT). However, it is still unknown which types of GB features are beneficial for thermoelectrics due to the challenge of correlating complex GB microstructures with transport properties. Here, it is demonstrated that GB complexions formed by Ga segregation in GeTe-based alloys can optimize electron and phonon transport simultaneously. The Ga-rich complexions increase the power factor by reducing the GB resistivity with slightly improved Seebeck coefficients. Simultaneously, they lower the lattice thermal conductivity by strengthening the phonon scattering. In contrast, Ga_2Te_3 precipitates at GBs act as barriers to scatter both phonons and electrons and are thus unable to improve ZT . Tailoring GBs combined with the beneficial alloying effects of Sb and Pb enables a peak ZT of ≈ 2.1 at 773 K and an average ZT of 1.3 within 300–723 K for $\text{Ge}_{0.78}\text{Ga}_{0.01}\text{Pb}_{0.1}\text{Sb}_{0.07}\text{Te}$. The corresponding thermoelectric device fabricated using 18-pair p-n legs shows a power density of 1.29 W cm^{-2} at a temperature difference of 476 K. This work indicates that GB complexions can be a facile way to optimize electron and phonon transport, further advancing thermoelectric materials.


footprint.^[1–4] The heat-to-electricity conversion efficiency depends on the dimensionless figure-of-merit of materials, defined as $ZT = S^2\sigma T/\kappa$, where S , σ , and T are the Seebeck coefficient, the electrical conductivity, and the absolute temperature, respectively. The total thermal conductivity (κ) consists of the electronic thermal conductivity (κ_e) and the lattice thermal conductivity (κ_l). The ZT value is directly proportional to several physical parameters summarized in the so-called materials quality factor, $B \propto \mu_w/\kappa_l$, at a given carrier concentration (n), where the weighted mobility (μ_w) and κ_l are determined by the transport properties of electrons and phonons, respectively.^[5] Hence, it is desirable to maximize the weighted mobility and minimize the lattice thermal conductivity. Yet, similarities in performance change of thermal and electrical transport for thermoelectrics impede the improvement of B factor for high ZT , which is the key challenge in optimizing TE materials.^[6]

1. Introduction

Thermoelectric (TE) materials can improve the efficiency of energy conversion by converting waste heat into electricity, showing considerable promise to reduce the carbon

Sustained efforts have been undertaken to improve the TE properties of materials, such as band convergence,^[7] resonant doping,^[8] energy filtering,^[9] high entropy,^[10] and hierarchical microstructure engineering.^[11] For polycrystalline bulk samples, the most ubiquitous defects are grain boundaries (GBs).

C. Zhang, G. Yan, Y. Wang, X. Wu, L. Hu, F. Liu, W. Ao
College of Materials Science and Engineering
Shenzhen Key Laboratory of Special Functional Materials
Shenzhen Engineering Laboratory for Advanced Technology of Ceramics
Guangdong Research Center for Interfacial Engineering of Functional Materials
Institute of Deep Underground Sciences and Green Energy
Shenzhen University
Shenzhen 518060, P. R. China
E-mail: zhangch@szu.edu.cn

 The ORCID identification number(s) for the author(s) of this article can be found under <https://doi.org/10.1002/aenm.202203361>.

© 2022 The Authors. Advanced Energy Materials published by Wiley-VCH GmbH. This is an open access article under the terms of the Creative Commons Attribution-NonCommercial License, which permits use, distribution and reproduction in any medium, provided the original work is properly cited and is not used for commercial purposes.

O. Cojocaru-Mirédin, M. Wuttig, Y. Yu
Institute of Physics (IA)
RWTH Aachen University
Sommerfeldstraße 14 52074, Aachen, Germany
E-mail: yu@physik.rwth-aachen.de

M. Wuttig
Peter Grünberg Institute—JARA-Institute Energy-Efficient Information Technology (PGI-10)
Forschungszentrum Jülich GmbH
52428, Jülich, Germany

G. J. Snyder
Department of Materials Science and Engineering
Northwestern University
Evanston, IL 60208, USA

DOI: 10.1002/aenm.202203361

This raises the question if they can be employed to improve the TE properties. It has been demonstrated that the increased GB phonon scattering in nanocrystalline BiSbTe bulk alloys greatly reduces κ , while maintaining μ_W , contributing to an improvement of ZT .^[12] In contrast, the increased fraction of GBs in Mg_3Sb_2 and half-Heusler alloys strongly impedes the charge carrier transport, diminishing μ_W and eventually even ZT .^[13,14] Therefore, it is still elusive which types of GBs can optimize the electron and phonon transport, leading to a simultaneous enhancement in μ_W and reduction in κ .

Grain boundaries possess complex microstructures and chemical compositions that can differ substantially from their adjacent grains.^[15,16] Improving the properties of materials through modifying these features of GBs is referred to as GB engineering. Driven by the reduced surface energy, impurity elements are prone to segregate to GBs as described by the Gibbs adsorption isotherm.^[17] These impurity atoms can also form GB precipitates once the thermodynamic and kinetic requirements of the nucleation and growth of a secondary phase are satisfied.^[18,19] GB segregation and precipitation impact the properties of materials by different mechanisms.^[20] The former is often described as a GB complexion that shows different GB microstructures and compositions at equilibrium,^[21] while the latter is a thermodynamically stable bulk phase with a certain crystal structure and stoichiometry. In thermoelectrics, both GB complexion and precipitation have been observed.^[22,23] Yet, the differences in controlling the TE properties by these distinct phenomena have been less studied.

Chalcogenides such as PbTe, AgSbTe₂, and Bi₂Te₃ show outstanding TE properties due to their unconventional chemical bonding mechanism, coined metavalent bonding, which differs considerably from ionic, metallic, and covalent bonding.^[24,25] Metavalent bonding is characterized by a unique property portfolio, such as large electronic polarizability and anharmonic bonds,^[26] as well as an unconventional bond rupture.^[27] Instead of electron pairs between adjacent atoms, only half an electron pair, thus in sum only one electron is shared between adjacent atoms.^[28] Crystalline GeTe also utilizes metavalent bonding and thus shows intrinsic outstanding TE properties.^[29,30] GeTe has attracted the attention in thermoelectrics since the 1960s,^[31,32] which was then utilized in the form of GeTe-AgSbTe₂ alloy (TAGS) by NASA. The ZT value of GeTe-based compounds has been improved from about 0.8 to above 2.0 by doping with Sb,^[33–36] Bi,^[37–39] Pb,^[38,40,41] and Mn,^[42,43] etc., showing great potential in mid-temperature power generation. Moreover, it has been demonstrated that the TE and mechanical properties of GeTe can be further improved by modifying its GB features via doping.^[44] Nevertheless, the study on the role of GBs in controlling the TE properties of GeTe is still in its infancy. Many issues such as the arrangement of dopants at GBs, i.e., the formation of complexions or precipitations, and their impact on TE performance have not yet been unraveled.

This work aims to explore the impact of different types of GB features on electron and phonon transport. To reach this goal, we systematically varied the content of Ga in a GeTe matrix. We choose Ga to decorate the GB because of the low solubility of Ga in GeTe^[45] and the large atomic mobility of Ga that promotes its spread along GBs.^[46] We found that a GB complexion with slight Ga enrichment was created by introducing 1 at%

Ga. Further increasing the content of Ga enables the formation of Ga₂Te₃ GB precipitates. Measurements of relevant transport properties demonstrate the ability of GB complexions in optimizing the electron and phonon transport synergetically, causing a simultaneous increase in μ_W and a decrease in κ . As a consequence, a high peak ZT of ≈ 2.1 at 773 K and an average ZT of ≈ 1.3 in the temperature range from 300 to 773 K are obtained in Ge_{0.78}Ga_{0.01}Pb_{0.1}Sb_{0.07}Te. In contrast, the formation of GB precipitates enhances phonon scattering yet shows a large GB resistance and thus has no net beneficial effects on the final TE performance. Moreover, the introduction of GB complexions along with Pb and Sb dopants dramatically reduce the difference in the thermal expansion coefficient before and after the phase transition of GeTe at about 600–700 K, enabling a robust TE device with a maximum output power density of 1.29 W cm⁻² at a temperature difference of 476 K.

2. Results and Discussion

2.1. Effects of Ga Doping on Tuning the TE Properties of GeTe-Based Alloys

Samples with nominal compositions of Ge_{0.9-x}Ga_xSb_{0.1}Te were synthesized to reveal the effect of Ga doping on modifying the TE properties of GeTe-based alloys. The content of Sb was fixed at 10 at% to optimize the background carrier concentration (n) as generally adopted for GeTe compounds.^[44,47,48] Figure 1a shows that the S increases with increasing the Ga content and temperature below 500 K and reaches the Golden range at high temperatures.^[49] In contrast, the σ first increases by adding 1% Ga and then decreases with further increasing the content of Ga (Figure 1b). The inflection points in Figure 1a,b at about 500 K cannot be attributed to the intrinsic excitation, which will cause an increase in the value of $\kappa - \kappa_e$ due to the strong bipolar effect. Yet, the $\kappa - \kappa_e$ decreases monotonously with temperature, as shown in Figure 1e. The phase transition of GeTe-based compounds from rhombohedral to cubic structures may already start at about 500 K for part of the grains. The cubic phase shows a higher carrier concentration^[50] and electrical conductivity than the rhombohedral phase, leading to decreased Seebeck coefficients and increased electrical conductivities with temperatures above 500 K. Once the phase transition is finished at about 600 K, the electrical conductivity decreases again with temperature due to the acoustic phonon scattering. The hole n decreases with the addition of Ga, especially when the content of Ga is greater than 2 at% (Figure S1, Supporting Information), which should be attributed to the weak n-type doping effect of Ga and the suppression of Ge vacancies^[51] from excess nominal Ge in the matrix by forming Ga₂Te₃ at the GB, as discussed below. Interestingly, the Ge_{0.9-x}Ga_xSb_{0.1}Te sample with $x = 1\%$ shows a simultaneous enhancement in S and σ over the entire temperature range measured (Figure 1c) compared to the Ga-free sample, leading to improved power factors ($PF = S^2\sigma$). In contrast, the PF values of samples with $x > 1\%$ do not show an obvious enhancement and are even slightly lower than that of pristine Ge_{0.9}Sb_{0.1}Te above 500 K. This is a typical tradeoff between the increased S and the decreased σ . These results indicate that the electrical transport properties are sensitive to

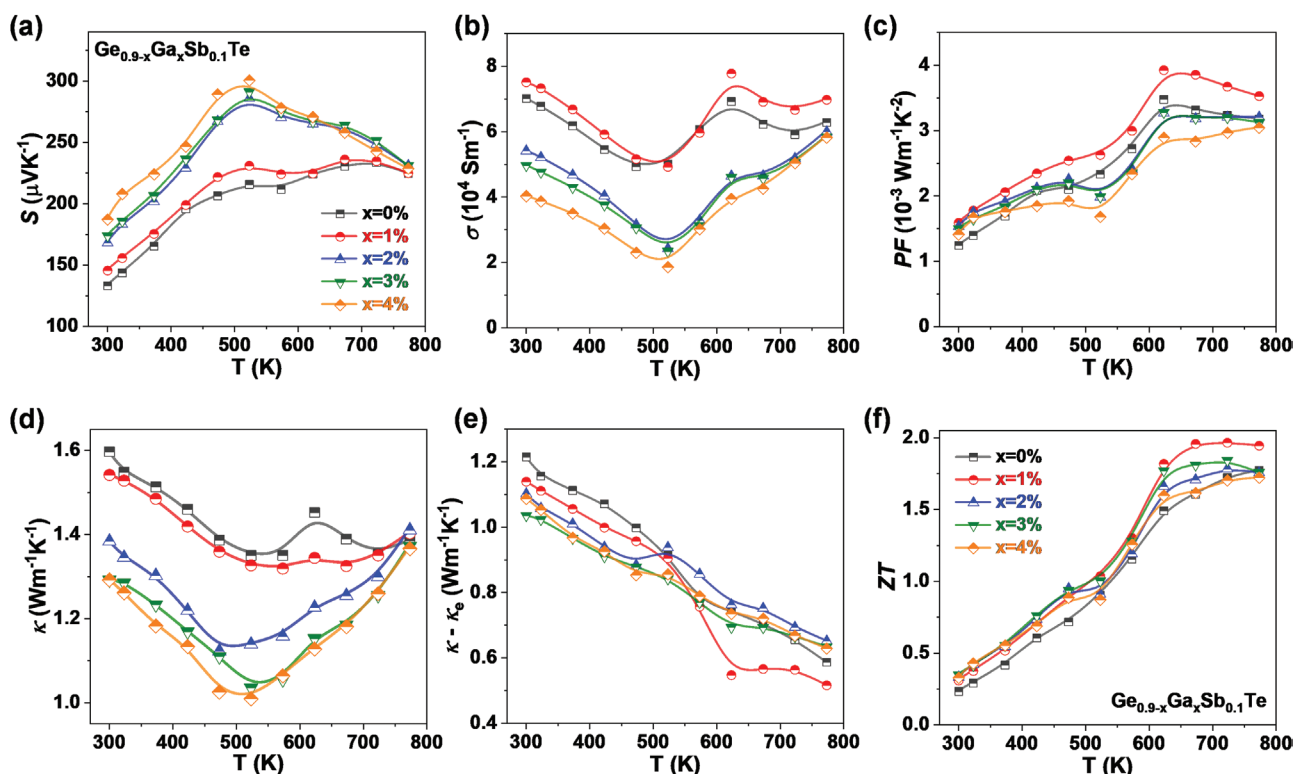


Figure 1. The effects of Ga doping on tuning the thermoelectric properties of $\text{Ge}_{0.9-x}\text{Ga}_x\text{Sb}_{0.1}\text{Te}$. Temperature-dependent a) S , b) σ , c) PF , d) κ , e) $\kappa - \kappa_e$, and f) ZT for the $\text{Ge}_{0.9-x}\text{Ga}_x\text{Sb}_{0.1}\text{Te}$ samples. All the figures share the same legend.

the content of Ga. While $x = 1\%$ Ga can enhance the S and σ simultaneously, a further increase in Ga content does not provide further gains in PF .

Figure 1d shows that κ decreases monotonously with increasing Ga content. The upward trend of κ over 500 K is mainly due to the increased σ with temperature. While a moderate decrease in κ can be observed in the sample $x = 1\%$, a much more significant reduction can be obtained in samples $x = 2\%$, 3% , and 4% , compared with the Ga-free counterpart. The abrupt change in the transport properties from sample $x = 1\%$ to samples $x = 2\text{--}4\%$ seems to be induced by a phase equilibrium change which would be related to phase boundary mapping,^[52] which can be further evidenced by the discontinuity in lattice parameters (Figure S2, Supporting Information). A small deviation of the composition of Ga induces very different microstructures and hence properties. The discontinuity in structures and properties is the hallmark of a complex transition.^[53]

The κ_l is determined by subtracting κ_e from κ , $\kappa_l = \kappa - \kappa_e = \kappa - L\sigma T$, and the Lorenz number L is estimated using an empirical formula,^[54] $L = 1.5 + \exp(-|S|/116)$, where S is in the unit of $\mu\text{V K}^{-1}$ and L is in $10^{-8} \text{ W } \Omega^{-1} \text{ K}^{-2}$. Compared with the $x = 1\%$ sample, the high-Ga samples ($x = 2\text{--}4\%$) show smaller κ_l in the low-temperature range ($<500 \text{ K}$) but larger κ_l in the high-temperature range ($>500 \text{ K}$) (Figure 1e). This can be ascribed to different scattering effects of structural defects on phonons, as will be elaborated below. Owing to the synergistic effects of doping Ga on increasing PF and reducing κ_l , the ZT of the $\text{Ge}_{0.89}\text{Ga}_{0.01}\text{Sb}_{0.1}\text{Te}$ sample ($x = 1\%$) can be enhanced

to a peak value of ≈ 1.97 at 723 K (Figure 1f). We also prepared $\text{Ge}_{0.9-x}\text{Ga}_x\text{Sb}_{0.1}\text{Te}$ samples with a smaller interval of Ga contents (Figure S3, Supporting Information), further demonstrating that simultaneous optimization of electron and phonon transport can be achieved in the samples with $x \leq 1\%$, while low thermal conductivity and high resistivity are observed synchronously in samples with $x > 1\%$ (see Figure 1b,e; and Figure S3, Supporting Information).

2.2. Further Improvement of ZT by Alloying Pb Based on the Beneficial Effect of Ga Doping

Based on the beneficial effect of Ga on optimizing the electron and phonon transport simultaneously, we further introduced Pb alloying to promote band convergence and reduction of κ_l . According to literature,^[40,44,55,56] the content of Pb was fixed at 10% and the carrier concentration was optimized by tuning the Sb and Ge content. We introduced 4% cation vacancies to optimize the carrier concentration. This can also assure that the observed differences in properties stem from the distinct GB features rather than the carrier concentration effect. Details of the TE properties can be found in Figure S4 (Supporting Information). We calculated the μ_W using the numerical equation described by Snyder et al.^[5] Though the pristine GeTe displays high μ_W values at low temperatures (Figure 2a), its PF has not been optimized due to its excessively high n related to its metavalent bonding nature.^[57] In addition, Figure 2b shows that the κ_l of pristine GeTe is too high to be a good TE material, especially at low temperatures. Alloying

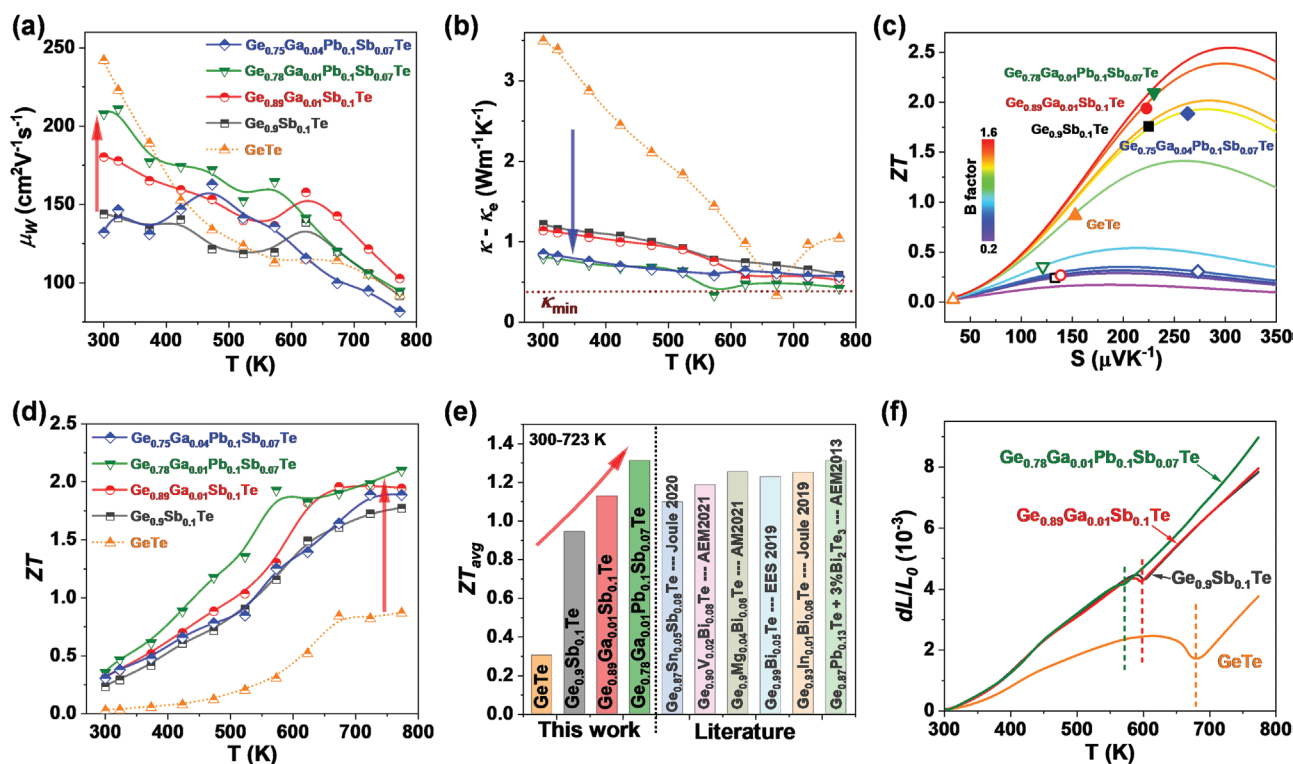


Figure 2. Progressive property improvements of GeTe by introducing Sb, Ga, and Pb, as well as the effect of different Ga content on corresponding properties. Temperature-dependent a) μ_W and b) $\kappa - \kappa_0$, c) S and B factor dependent ZT , d) temperature-dependent ZT , e) average ZT in the range of 300–723 K, and f) temperature-dependent relative length variation (dL/L_0) for the samples of GeTe, $\text{Ge}_{0.9}\text{Sb}_{0.1}\text{Te}$, $\text{Ge}_{0.89}\text{Ga}_{0.01}\text{Sb}_{0.1}\text{Te}$, $\text{Ge}_{0.78}\text{Ga}_{0.01}\text{Pb}_{0.1}\text{Sb}_{0.07}\text{Te}$, and $\text{Ge}_{0.75}\text{Ga}_{0.04}\text{Pb}_{0.1}\text{Sb}_{0.07}\text{Te}$. Symbols with open and solid shapes in (c) represent the data at 300 and 773 K, respectively. Average ZT s from the literature [35,59–63] are also listed for comparison in (e).

Sb can effectively optimize the n and reduce the κ_1 (Figure 2b) despite the decreased μ_W . Adding Ga can further enhance μ_W and diminish κ_1 . This beneficial effect is strengthened by alloying Pb. However, further increasing the Ga-doping level deteriorates μ_W and PF , which is akin to the Pb-free case (Figure 1). The striking difference in transport of charge and heat is indifferent to the presence of Pb but strongly depends on the content of Ga.

As displayed in Figure 2c, the quality factor, B , which describes the net effect of increased μ_W and/or decreased κ_1 , is calculated by Equation (1)^[5]

$$B = \left(\frac{k_B}{e} \right)^2 \frac{8\pi e (2m_e k_B T)^{3/2}}{2h^3} \frac{\mu_W}{\kappa_1} T \quad (1)$$

The open and closed symbols in Figure 2c represent data obtained at 300 and 773 K, respectively. A stepwise increase in the B factor is achieved in the GeTe-based compounds by progressively introducing Sb, Ga, and Pb (Figure 2c). However, a higher Ga-doping level adversely decreases the B factor. A maximum ZT of 2.5 can be predicted for sample $\text{Ge}_{0.78}\text{Ga}_{0.01}\text{Pb}_{0.1}\text{Sb}_{0.07}\text{Te}$, while only a maximum ZT of 1.9 is achievable for sample $\text{Ge}_{0.75}\text{Ga}_{0.04}\text{Pb}_{0.1}\text{Sb}_{0.07}\text{Te}$ by optimizing the n while keeping B . The obtained B factor is comparable to other GeTe-based compounds doped with Ta, V, Cu, Cd, and I.^[58]

As summarized in Figure 2d, the enhancement of ZT follows the trend of the B factor depending on the doping elements. Introducing appropriate Ga (1%) in conjunction with the

optimization of n by Sb alloying is quite efficient in enhancing ZT at high temperatures while substituting Ge by Pb is especially useful for improving ZT in the lower temperature range. It is also worth noting that a higher doping level of Ga is detrimental to ZT and even counteracts the beneficial effect of Pb alloying. The optimal $\text{Ge}_{0.78}\text{Ga}_{0.01}\text{Pb}_{0.1}\text{Sb}_{0.07}\text{Te}$ sample shows a high ZT of ≈ 0.36 at 300 K and a peak ZT of ≈ 2.1 at 773 K. Generally, a large average ZT (ZT_{avg}) is more important than the peak ZT in terms of the energy conversion efficiency. We compared the ZT_{avg} of our samples with other representative GeTe-based compounds in the range of 300–723 K, as shown in Figure 2e. The highest ZT_{avg} value of 1.31 was obtained in $\text{Ge}_{0.78}\text{Ga}_{0.01}\text{Pb}_{0.1}\text{Sb}_{0.07}\text{Te}$, which outperforms many GeTe-based alloys reported in the literature,^[35,59–63] though higher ZT_{avg} values have also been achieved recently.^[10,64,65]

Besides TE performance, thermal stability is also a critical factor for obtaining high-performance and durable TE devices, especially for GeTe-based alloys with a phase-transition behavior. Figure 2f shows the temperature-dependent relative length variation (dL/L_0), where the slope of corresponding curves indicates the coefficient of thermal expansion (CTE). The CTE of pristine GeTe shows an abrupt change near the phase-transition temperature (≈ 673 K), which could cause cracks in the materials and even failure of the TE devices. Introducing Pb, Sb, and Ga can almost eliminate the abrupt change in CTE, due to the improved symmetry of the low-temperature GeTe phase by multicomponent alloying that reduces the structure

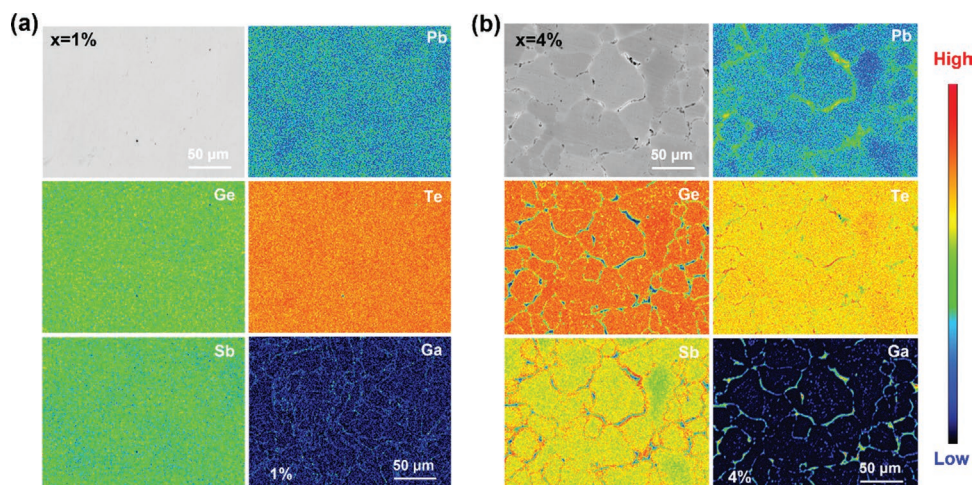


Figure 3. Electron probe microanalyzer (EPMA) characterizations. EPMA images of samples and relevant elemental mapping of Pb, Ge, Te, Sb, and Ga for the $\text{Ge}_{0.79-x}\text{Ga}_x\text{Pb}_{0.1}\text{Sb}_{0.07}\text{Te}$ samples with a) $x = 1\%$ and b) $x = 4\%$ Ga doping level.

mismatch during phase transition.^[47] This smooth evolution of CTE at phase transition enables the $\text{Ge}_{0.78}\text{Ga}_{0.01}\text{Pb}_{0.1}\text{Sb}_{0.07}\text{Te}$ more favorable for the assembly and application of TE devices.

We also repeated the measurement of TE properties of $\text{Ge}_{0.89}\text{Ga}_{0.01}\text{Sb}_{0.1}\text{Te}$ and $\text{Ge}_{0.78}\text{Ga}_{0.01}\text{Pb}_{0.1}\text{Sb}_{0.07}\text{Te}$, both showing good reproducibility (Figure S5, Supporting Information). It is important to note that the optimization window of the Ga content on tuning the TE properties of GeTe is very narrow. A performance improvement can only be achieved at the Ga content of $\leq 1\%$, when complexions form, independent of the presence or absence of Pb. This phenomenon calls for an explanation from the perspective of microstructures and their impact on the transport of charge and heat.

2.3. Grain-Boundary Ga Complexions Versus Precipitations

Structural characterizations are performed to understand the effect of Ga doping on tuning the TE properties of GeTe-based alloys. **Figure 3** displays the electron probe microanalyzer (EPMA) mappings of samples with different Ga doping levels. At a low Ga doping content (1%), the Ga element tends to segregate at GBs while the other elements like Pb, Ge, Te, and Sb are almost uniformly distributed (Figure 3a). At a higher Ga doping level (4%), a much more obvious enrichment of Ga at GBs is observed with concomitant enrichment of Te and deficiency of Ge and Sb (Figure 3b), suggesting the formation of secondary phases of Ga_2Te_3 , as further confirmed by point scanning on these secondary phases (Figure S6, Supporting Information). These precipitates consume Te from the GeTe matrix and then some Pb atoms must be repelled to the GB area to keep charge balance within the grain. The enrichment of Ga at GBs can be further evidenced by an etching treatment combined with elemental mapping (Figures S7 and S8, Supporting Information). Our theoretical calculations also suggest that the Ga segregation in GeTe is energetically favorable (Figure S9, Supporting Information). It is striking that 10% Pb and Sb can be miscible in the GeTe matrix while even 1% Ga generates observable segregation. Note that all the Pb, Sb, and Ga mainly occupy the Ge lattice.

The most stable compounds formed by these elements with Te are PbTe , Sb_2Te_3 , and Ga_2Te_3 . Strikingly, Ga_2Te_3 is the only one that utilizes a different chemical bonding mechanism (covalent), while both PbTe and Sb_2Te_3 employ the same chemical bonding mechanism as the GeTe matrix (metavalent).^[26,30] The different chemical bonding mechanisms might explain the distinct solubility of different elements in GeTe and the formation of Ga segregations and precipitations.^[66] As suggested in Figure 3, Pb and Sb with high solubility in GeTe mainly impact the properties of the matrix. In contrast, Ga-related segregation or precipitation especially impacts the charge and heat transport at GBs.

We then performed atom probe tomography (APT) measurements to better reveal the distribution of Ga at GBs and inside the grains. This technique shows a much higher spatial resolution (sub-nanometer scale) and chemical sensitivity (ppm level) than that of EPMA and is particularly important for investigating GB microstructures.^[13,67–69] Besides, it provides information about the bond-rupture behavior and thus can distinguish meta-valent bonding from other chemical bonding mechanisms.^[27,70] **Figure 4a** shows a homogeneous distribution of Ge, Sb, Pb, and Te in 3D space for the sample $x = 1\%$. In contrast, Ga-rich clusters and Ga segregation to a GB can be observed, indicating a small solubility of Ga in GeTe. The linear composition profile across the GB as indicated by an arrow quantifies the partition coefficient of Ga to the GB as a factor of about 10 (Figure 4b). Yet, the absolute content of Ga at the GB is about 1.0 at%, which is still far away from any Ga-related thermodynamically stable bulk phases. In this regard, the GB area decorated by Ga is referred to as GB complexions.^[21] Besides the GB complexions, Figure 4c shows the composition proximity histogram of a Ga-rich cluster depicted by an isosurface of 1.5 at% Ga. The chemical composition of the matrix is very close to the nominal stoichiometry except for the much lower solubility of Ga than expected. The content of Ga can reach as high as about 5 at% in the core of the Ga-rich cluster. Extra insoluble Ga has to be expelled from the matrix to form GB complexions.

We further analyzed the sample $x = 4\%$ using APT for a better comparison of the Ga distribution. **Figure 5a** shows the 3D distribution of elements measured with a needle-shaped specimen as illustrated in Figure 5b. A distinct contrast between

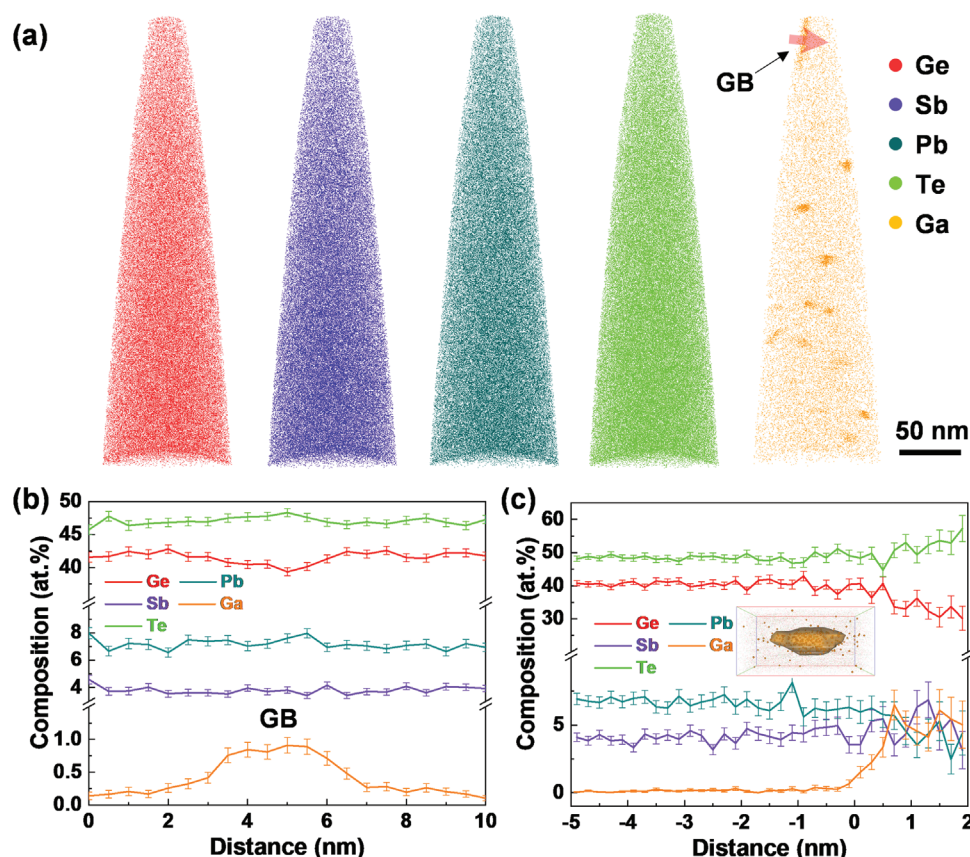


Figure 4. Atom probe tomography (APT) reconstruction showing the elemental distributions and composition analyses for sample $x = 1\%$. a) 3D distributions of Ge, Sb, Pb, Te, and Ga; each element is represented by a specific color. b) Linear composition profile across a GB indicated by an arrow in the 3D map; Ga enrichment at the GB is detected. c) Composition proximity histogram calculated across an iso-composition surface of 1.5 at% Ga, as depicted in the inset; negative and positive distances mean the surrounding matrix and the Ga-rich cluster interior, respectively.

the middle layer and its two adjacent layers can be observed under the scanning electron microscope (SEM), indicating different compositions. This middle layer with a bright contrast is determined to be Ga_2Te_3 , while the top and bottom materials are GeTe. This sandwiched structure is consistent with the EPMA results in Figure 3b. The top GeTe grain was successfully measured in APT. A similar distribution of all the elements compared with the sample $x = 1\%$ is reconstructed. Unfortunately, the interface between GeTe and Ga_2Te_3 was not detected by APT due to the abrupt change of the evaporation field that leads to the rupture of the APT specimen.^[68] Nevertheless, the nature of a thermodynamically stable secondary bulk phase has been revealed by EPMA (Figure 3b) and elemental scanning (Figure S6, Supporting Information). This is very different from the GB complexions formed in the sample with a lower Ga content ($x = 1\%$). The atomic distributions of the Ga-rich cluster are magnified in Figure 5c. The chemical composition of the Ga-rich cluster is also consistent with that observed in the sample $x = 1\%$, which implies a saturation of the Ga content in the cluster (Figure 5d). Thus, the major difference between samples $x = 1\%$ and $x = 4\%$ is the GB feature. The former creates GB complexions while the latter forms GB precipitates.

More evidence of the transition from GB complexions to GB precipitates can be inferred from the average grain size of the

GeTe matrix. Figure S10 (Supporting Information) shows that the average grain size first decreases from $8.96 \mu\text{m}$ for the Ga-free sample to $5.23 \mu\text{m}$ for sample $x = 1\%$ and then increases to $9.50 \mu\text{m}$ for sample $x = 4\%$. According to the Gibbs adsorption isotherm and McLean's GB segregation model,^[71,72] the GB energy γ can be expressed as

$$\gamma = \gamma_0 - \Gamma (RT \ln X + \Delta H^{\text{seg}}) \quad (2)$$

where γ_0 is the GB energy without segregation, R is the gas constant, T is the aging temperature, X is the dopant fraction in the lattice, ΔH^{seg} is the enthalpy of segregation, and Γ is the Gibbsian interfacial excess of solute at interfaces. The enrichment of Ga at the GB ($\Gamma > 0$) revealed by APT (Figure 4b) qualitatively implies that the total GB energy must be decreased due to the formation of GB complexions. In this regard, the driving force for grain growth is diminished and thereby a smaller grain size is obtained in the sample $x = 1\%$. In contrast, once the transition from GB complexions to GB precipitation occurs, the grains grow at elevated temperatures. This is because the solute Ga atoms no longer lower the GB free energy by occupying GB sites but form a precipitate. A similar effect has been observed in nanocrystalline Ni-P alloys, where the grain size increases due to the precipitation of the equilibrium Ni_3P phase.^[73] The

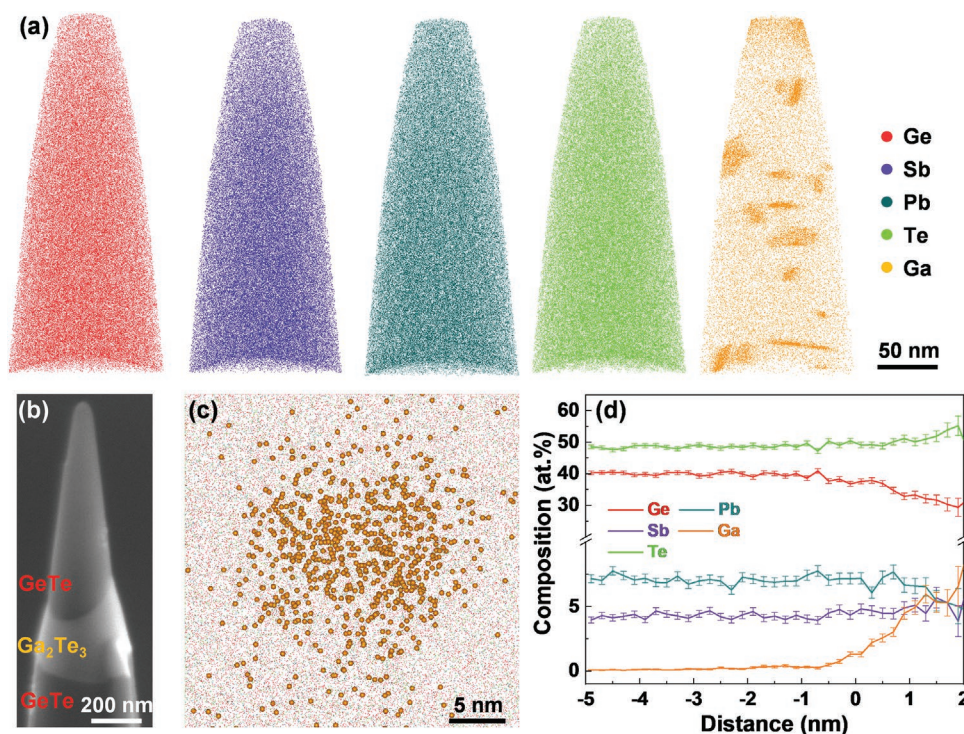


Figure 5. APT reconstruction showing the elemental distributions and composition analyses for sample $x = 4\%$. a) 3D distributions of Ge, Sb, Pb, Te, and Ga. b) Needle-shaped APT specimen illustrating a sandwiched structure with the middle layer as Ga_2Te_3 and the top and bottom layers as GeTe. c) Close-up of a Ga-rich cluster. d) Composition proximity histogram calculated across an iso-composition surface of 1.5 at% Ga; negative and positive distances mean the surrounding matrix and the Ga-cluster interior, respectively.

different grain sizes between samples $x = 1\%$ and $x = 4\%$ corroborate the observations by APT that the former forms GB complexions, while the latter transforms into GB precipitates.

2.4. Distinct Roles of GB Complexions and Precipitations on the Electron and Phonon Transport

To further understand the Ga doping effects on the electronic transport of GeTe, we performed density functional theory (DFT) calculations using moderate-size cubic $\text{c-Ge}_{27}\text{Te}_{27}$ and rhombohedral $\text{r-Ge}_{27}\text{Te}_{27}$ as basis GeTe supercells. Though Ga dopant shows quite limited solubility in the GeTe matrix as revealed by APT, the DFT calculations of Ga-doped samples ($\text{c-Ge}_{26}\text{Ga}_1\text{Te}_{27}$, $\text{r-Ge}_{26}\text{Ga}_1\text{Te}_{27}$) can be employed to roughly reveal the electronic structures of the Ga-rich GB complexions. Because of the p-type transport behaviors, the valence band (VB) determines the electronic transport properties of GeTe. We also performed band-unfolding calculations on these supercells, which enable direct comparison with those primitive cells. As shown in **Figure 6a**, Ga doping can dramatically induce split-off bands from the VB maximum (VBM), which also changes the total density of states (DOS) accordingly (Figure 6b). In comparison with the pristine cubic GeTe ($\text{c-Ge}_{27}\text{Te}_{27}$), the Ga-doped GeTe ($\text{c-Ge}_{26}\text{Ga}_1\text{Te}_{27}$) shows a narrow plateau DOS near VBM. The Ga-projected DOS nearly shares the same energy location with the plateau DOS, which comprises $\approx 10\%$ of the Ga-projected DOS. The Ga-induced distortion of bands and DOS near VBM can be

mainly ascribed to the interaction between Ga-4s and Te-5p, Ge-4s and Ge-4p orbitals (Figure S11, Supporting Information), which is also understood as the “resonant level” in previous reports.^[74] In rhombohedral phases (Figure 6c), the difference between $\text{r-Ge}_{27}\text{Te}_{27}$ and $\text{r-Ge}_{26}\text{Ga}_1\text{Te}_{27}$ in DOS is quite similar to that in cubic phases (Figure 6b), though rhombohedral GeTe shows a larger bandgap than cubic GeTe due to Peierls distortion.^[25] As reflected from the total DOS, the Ga doping also shrinks the bandgap of GeTe due to the formation of impurity states. We also included the Pb or Sb element in the DFT calculations (Figure S12, Supporting Information) and found that the “resonant level”-like behavior of Ga doping is nearly independent of the presence of Pb or Sb.

We use a two-phase model proposed by Kuo et al.^[75] to understand the distinct roles of GB complexions and precipitations on the transport properties, where the overall S and σ are determined by

$$\sigma^{-1} = (1 - t_{\text{GB}})\sigma_{\text{G}}^{-1} + t_{\text{GB}}\sigma_{\text{GB}}^{-1} \quad (3)$$

$$S \approx S_{\text{G}} \quad (4)$$

The subscripts G and GB represent the contribution from the grain and the GB phase, respectively, and t_{GB} is the size fraction of the GB phase. For the GB complexions, owing to the shrinkage of the bandgap by Ga doping, the valence band bends upward which behaves as a conducting layer for p-type semiconductors, as sketched in Figure 6d. Therefore, high

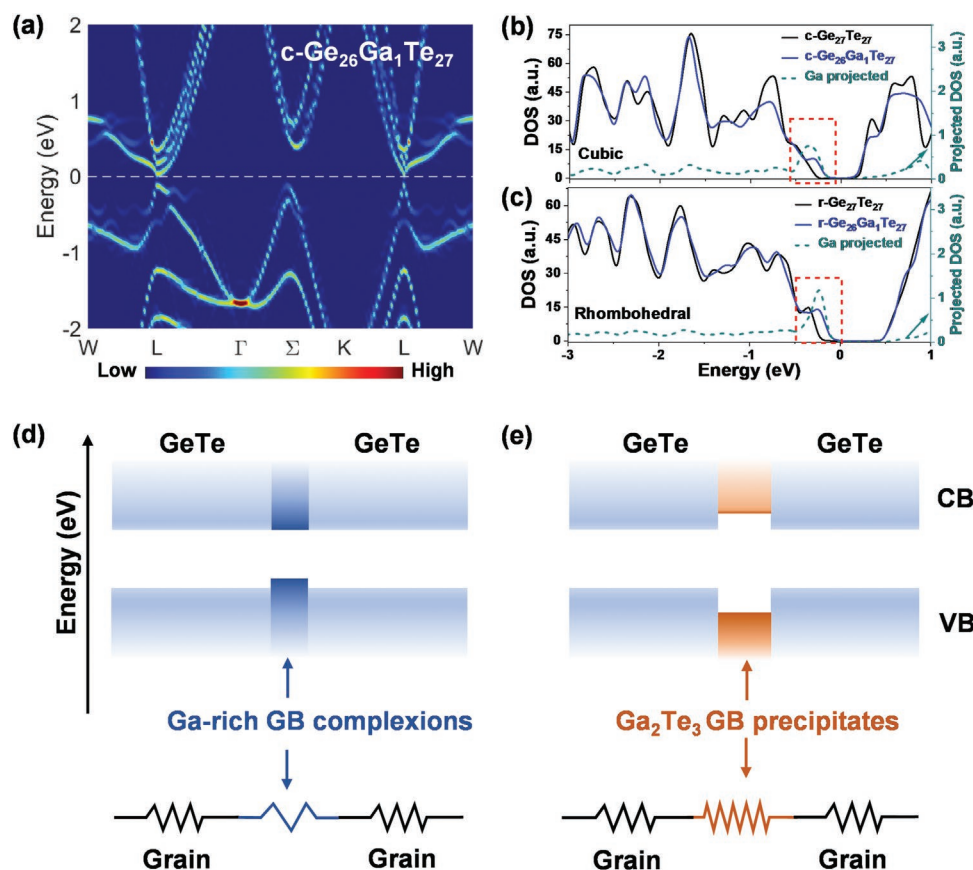


Figure 6. Density functional theory (DFT) calculations. a) The unfolded band structure of c-Ge₂₆Ga₁Te₂₇, where the color highlights the weight of bands. b) The density of states (DOS) of the cubic Ge₂₇Te₂₇ and Ge₂₆Ga₁Te₂₇. c) DOS of rhombohedral Ge₂₇Te₂₇ and Ge₂₆Ga₁Te₂₇. The Ga-projected DOS is also displayed in (b,c). Schematic band structures and series circuit models near grain boundaries (GBs) when the d) Ga-rich complexions and e) Ga₂Te₃ precipitates are the dominant GB features, respectively. The CB and VB represent the conduction band and valence band, respectively. The sketch is drawn based on DFT calculations but not to scale regarding the relative energy levels. The calculated bandgap for Ga₂Te₃ (≈ 0.59 eV) is larger than that for GeTe (≈ 0.27 eV for c-GeTe, ≈ 0.35 eV for r-GeTe) and the calculated Fermi energy for Ga₂Te₃ (≈ 4.04 eV) is much lower than that for c-GeTe (≈ 6.08 eV). Due to the equilibrium of the Fermi energy levels, the valence band bends downward.

σ_{GB} will lead to a higher σ in line with the experimental data (Figure 1b). In conjunction with the increase of DOS near VBMs, the Ga-rich GB complexions lead to the simultaneous increase of S and σ in the sample with a low Ga doping level ($x = 1\%$) (Figure 1a,b). In striking contrast, a high GB resistance, i.e., a small σ_{GB} , is obtained in samples with Ga₂Te₃ precipitates (e.g., $x = 4\%$) because of the intrinsic poor electrical conductivity of Ga₂Te₃ and the energy band misalignment at the interface forming a potential barrier (Figure 6e). Therefore, deteriorated electrical properties in samples with high Ga content are observed (Figure 1a–c).

Regarding the thermal transport properties, both the GB complexions and precipitations reduce the κ_i by introducing the Kapitza resistance.^[72,76] The Ga atoms that occupy nonperiodic sites at the GB complexions are equivalent to point defects, which scatter high-frequency phonons. This explains the lower κ_i for sample $x = 1\%$ at higher temperatures (Figure 1e). In addition, the long fragment of complexions that resembles a normal interface can scatter low-frequency phonons. In conjunction with the increased electrical properties discussed above, it is fair to say that the GB complexions optimize the electron and phonon transport simultaneously, leading to a large enhancement of the B factor. In contrast, the formation of

a bulk precipitate phase at the GB can no longer be considered a complexion. This precipitate phase strongly impedes the transport of low-frequency phonons due to the acoustic mismatch induced by the distinct chemical bonding mechanisms between GeTe (metavalent bonding) and Ga₂Te₃ (covalent bonding).^[70] This is responsible for the lower κ_i for samples $x > 1\%$ near room temperature (Figure 1e) because the boundary phonon scattering is often effective at low temperatures. Nevertheless, the increased Kapitza resistance is compensated for by the decreased GB electrical conductivity. As a consequence, the formation of GB precipitates is less effective or even detrimental in improving ZT than the GB complexions. Given the large average grain size (5.23 μm , Figure S10, Supporting Information) for the 1% Ga sample, the effect of GB complexions on simultaneously optimizing electron and phonon transport is quite considerable. Our work exemplifies the feasibility of this strategy, which could be prominent in nanostructures.

2.5. Robust Thermoelectric Device and High Output Power

We fabricated an 18-pair TE device using Ge_{0.78}Ga_{0.01}Pb_{0.1}Sb_{0.07}Te as p-type legs and Yb_{0.3}Co₄Sb₁₂ (Figure S13, Supporting

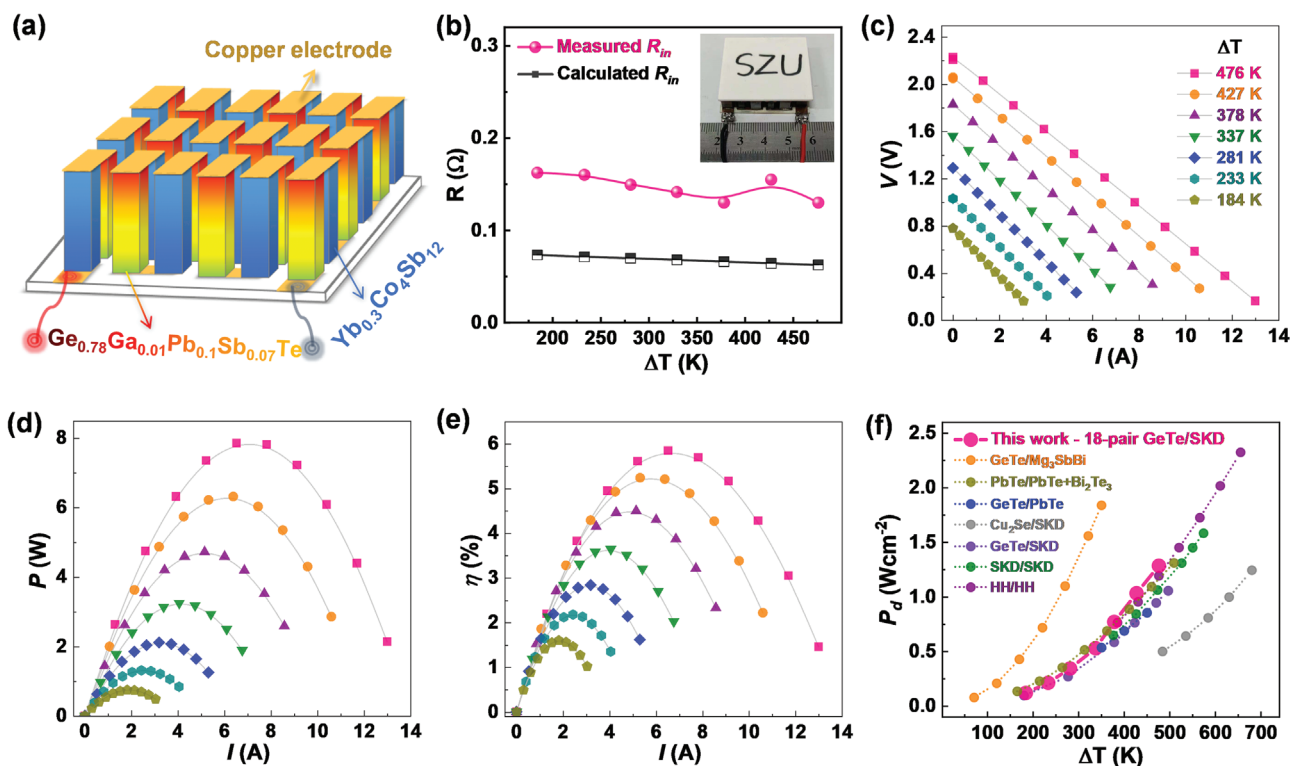


Figure 7. GeTe-based thermoelectric device. a) Schematic structure of an 18-pair $\text{Ge}_{0.78}\text{Ga}_{0.01}\text{Pb}_{0.1}\text{Sb}_{0.07}\text{Te}/\text{Yb}_{0.3}\text{Co}_4\text{Sb}_{12}$ TE device. b) Measured internal resistance (R_{in}) and calculated R_{in} without considering the interfacial contact resistance, and the inset shows the optical image of our TE device. Current-dependent c) output voltage, d) output power, and e) energy conversion efficiency of the TE device under various temperature differences (ΔT). f) The output power density of our TE device under different ΔT and literature data of other TE devices presented for comparison,^[62,79–84] where SKD and HH represent skutterudites and half-Heusler alloys, respectively.

Information) as n-type legs, as illustrated in Figure 7a and the inset of Figure 7b. The device performance is measured by a commercial testing system (PEM-2), wherein the cold-site temperature is fixed at 283 K and the hot-side temperature is varied to obtain various temperature differences (ΔT). The internal resistance (R_{in}) of the device under ΔT of 184–476 K is measured to be 0.13–0.16 Ω , which is only slightly higher than the calculated resistance without considering the contact resistance. Therefore, the interfacial contact resistance is estimated to be only 0.06–0.09 Ω for our 18-pair TE module.

Owing to a large number of TE legs with outstanding TE performance in our device, the open-circuit voltage (V_{OC}) increases from 0.8 to 2.2 V with the ΔT increasing from 184 to 476 K (Figure 7c), exceeding the voltage level of a dry battery (1.5 V). The output voltage V declines linearly with the increase of current I (Figure 7c). Therefore, the output power P (Figure 7d) and the energy-conversion efficiency η (Figure 7e) at specific ΔT both gradually increase to peak values and then decline with the increase of I . The optimal current for peak P and η at specific ΔT is obtained when the external electrical load is identical to R_{in} . As a result, a maximum P of 7.86 W (corresponding to power density P_d of 1.29 W cm^{-2}) and a maximum η of 5.85% at $\Delta T = 476 \text{ K}$ and $I = 6.52 \text{ A}$ are achieved. Considering the radiant heat loss during the measurement,^[44] the η of our TE devices is somehow underestimated. This problem has also been discussed by other literature^[77,78] and in our previous report.^[44] Moreover, determining the heat flow by different

homemade setups can also raise the uncertainty of η . On the other hand, the P_d is nearly independent of the radiant heat and the measurement of heat flow, making it a robust parameter for comparing the performance of different TE devices. As shown in Figure 7f, except for the GeTe/Mg₃SbBi device,^[79] our P_d is comparable to or higher than other GeTe-based TE devices,^[62,80] as well as PbTe,^[81] skutterudites,^[82,83] and half-Heusler^[84] based TE devices. It is worth noting that our TE device has 18-pair TE legs, while other reported TE devices have only 8-pair legs or even a single leg, which show smaller contact resistance yet cannot generate sufficient output power for practical power-generation applications. Reducing the R_{in} , enhancing the TE performance of n-type legs (the n-type $\text{Yb}_{0.3}\text{Co}_4\text{Sb}_{12}$ used here only shows peak $ZT \approx 1$, Figure S13, Supporting Information), and optimizing the device structures are promising approaches to further improve the η and P_d of the GeTe-based TE devices.

3. Conclusions

In summary, we reported on a GB complexion formed by Ga segregation in GeTe-based alloys, which can simultaneously increase μ_W and reduce κ_l . Ga segregation at GB without forming secondary Ga_2Te_3 phases can form a thermoelectrically active complexion layer with a reduced bandgap and increased DOS, resulting in a synergistic enhancement of S and σ . In addition, the Ga-rich GB complexions enhance

the phonon scattering to reduce κ_l . In combination with the alloying effects from Sb and Pb, a peak ZT of ≈ 2.1 at 773 K and an average ZT of 1.31 within 300–723 K can be obtained in $\text{Ge}_{0.78}\text{Ga}_{0.01}\text{Pb}_{0.1}\text{Sb}_{0.07}\text{Te}$. This composition also shows a well-matched CTE before and after the phase transition, facilitating the assembly and durability of TE devices. We successfully fabricated an 18-pair GeTe-based device, showing P_d of 1.29 W cm^{-2} and η of 5.85% at $\Delta T = 476 \text{ K}$. Our work demonstrates that GB complexions formed by appropriate segregation could decouple the transport of electrons and phonons, enhancing the TE performance. However, the formation of GB precipitates due to over-doping can strongly impair the interfacial electrical properties and are thus not necessarily beneficial to the TE properties. There are clear doping limits for different elements and the mechanisms underpinning this difference in solubility should be of critical significance for doping by design. This work also provides insights into the microstructural complexity of the GB network that must be treated in detail to allow for tunable TE properties.

4. Experimental Section

Sample Preparations: Raw materials of Ge, Ga, Pb, Sb, and Te with a purity of 99.99% were stoichiometrically weighed to synthesize $\text{Ge}_{0.9-x}\text{Ga}_x\text{Sb}_{0.1}\text{Te}$ and other Ga-doped GeTe-based alloys described in the context. The weighed raw materials were then sealed in the vacuum quartz tube ($\approx 3 \times 10^{-3} \text{ Pa}$) and heated to 1050°C in 4 h, kept at 1050°C for 20 h, and then cooled to 600°C in 4 h. After holding at 600°C for 10 h, samples were slowly cooled to room temperature. The as-prepared ingots were hand-ground into powders using an agate mortar and pestle. The powders were loaded into a $\Phi 20 \text{ mm}$ graphite die and were then sintered into bulk pellets by a spark plasma sintering (SPS) system at 600°C for 8 min under an axial pressure of 40 MPa. Bulk pellets were cut into bar shapes of $13.0 \times 3.5 \times 3.5 \text{ mm}$ for the electrical measurements, and square shapes of $10 \times 10 \times 2 \text{ mm}$ for the thermal diffusivity measurements.

Characterization Methods: Electron probe microanalyzer (EPMA, JXA-8530F PLUS) equipped with wave dispersive spectrometer (WDS) was used for morphology and elemental analysis. Needle-shaped APT specimens were prepared by a dual-beam scanning electron microscopy/focused ion beam (SEM/FIB) (Helios NanoLab 650, FEI, USA) following the standard “lift-out” method. APT measurements were conducted on a local electrode atom probe (LEAP 4000X Si, Cameca, USA). The laser pulses were adapted with a wavelength of 355 nm, a pulse duration of 10 ps, and pulse energy of 15 pJ. A pulse repetition rate of 200 kHz with a detection rate of 1% on average, an ion flight path of 160 mm, and a specimen base temperature of 40 K were utilized. The APT data were processed using the commercial software package IVAS 3.8.0 from Cameca instruments.

The ZEM-2 apparatus (Ulvac-Riko) was used for the measurement of the Seebeck coefficient and electrical conductivity. The thermal conductivity κ was determined via the equation $\kappa = \lambda d C_p$, where the thermal diffusivity (λ) was measured by the laser flash diffusivity method (LFA-467, NETZSCH), and density (d) was measured by the Archimedes method, and the specific heat capacity (C_p) was determined by the Dulong-Petit law ($C_p = 3k_B$ per atom, k_B is the Boltzmann constant). The room-temperature Hall carrier density n was measured by the physical properties measurement system (PPMS, Quantum Design). The uncertainty of σ , S , and κ is estimated to be around $\pm 3\%$, $\pm 5\%$, and $\pm 5\%$, respectively. The error bars were not displayed to keep good readability.

Theoretical Calculations: The density functional theory (DFT) calculations were performed on supercell models of GeTe and Ga-doped GeTe using the Vienna Ab initio Simulation Package (VASP),^[85] where the Perdew–Burke–Ernzerh of exchange–correlation function (GGA–PBE) and

projector enhanced wave (PAW) type pseudopotentials were used.^[86,87] The cut-off energy of the plane-wave basis was set to 480 eV, and the energy convergence criterion was set as 10^{-6} eV per cell for the structural relaxations. A dense k -mesh of $5 \times 5 \times 5$ sampling with the Monkhorse–Pack mode^[88] was used. The spin–orbit coupling effects were also taken into account in determining the band structures and density of states. The VASPKIT software was also used to perform the band-unfolding calculations.^[89]

Thermoelectric Module Fabrication and Characterization: The SPS-derived samples $\text{Ge}_{0.78}\text{Ga}_{0.01}\text{Pb}_{0.1}\text{Sb}_{0.07}\text{Te}$ and $\text{Yb}_{0.3}\text{Co}_4\text{Sb}_{12}$ were used as p-type and n-type TE legs, respectively, which were then coated with the barrier layer ($\approx 20 \text{ nm}$) of Mo and Ti by magnetron sputtering (X-smart, SKY), respectively. The $\text{Ge}_{0.78}\text{Ga}_{0.01}\text{Pb}_{0.1}\text{Sb}_{0.07}\text{Te}/\text{Mo}$ and $\text{Yb}_{0.3}\text{Co}_4\text{Sb}_{12}/\text{Ti}$ were cut into p-type and n-type TE legs with geometric dimensions of $\approx 4.65 \text{ mm} \times 4.65 \text{ mm} \times 5.2 \text{ mm}$ and $\approx 2.65 \text{ mm} \times 4.65 \text{ mm} \times 5.2 \text{ mm}$, respectively. The 18-couple TE module was assembled with copper-clad plates using $\text{Ag}_{72}\text{Cu}_{28}$ solder paste. The output performance of the TE module was measured by a commercial TE-module testing system (PEM-2, Advance Riko) in a helium atmosphere. The cold site temperature T_c was maintained at 283 K by a recycled cooling setup, and then the hot site temperature T_h was increased to corresponding set values for the device test.

Supporting Information

Supporting Information is available from the Wiley Online Library or from the author.

Acknowledgements

This work was supported by Shenzhen Science and Technology Innovation Commission (Grant Nos. 20200731215211001 and 20200814110413001), Guangdong Basic and Applied Basic Research Foundation (Nos. 2022A1515012492 and 2022A1515011820), and Shenzhen Clean Energy Research Institute. Y.Y., O.C.-M., and M.W. acknowledge support from the German Research Foundation DFG within project SFB917. Y.Y. acknowledges the financial support under the Excellence Strategy of the Federal Government and the Länder within the ERS RWTH Start-Up grant (Grant No. StUpPD_392-21).

Open access funding enabled and organized by Projekt DEAL.

Conflict of Interest

The authors declare no conflict of interest.

Author Contributions

C.Z. and Y.Y. conceived this research. G.Y. and Y.W. prepared the samples and devices and conducted corresponding thermoelectric property measurements under the supervision of C.Z.. C.Z. finished the DFT calculations. Y.Y. carried out the APT experiments. C.Z. and Y.Y. analyzed the experimental data and wrote the manuscript. X.W., L.H., F.L., and W.A. contributed to the supervision, methodology, and resources. O.C.-M., M.W., and G.J.S. reviewed and edited the draft and provided helpful suggestions on the interpretation of data. All authors commented on the manuscript.

Data Availability Statement

The data that support the findings of this study are available from the corresponding author upon reasonable request.

Keywords

atom probe tomography, density functional theory, grain boundary complexation, metavalent bonding, thermoelectric devices

Received: October 5, 2022

Revised: November 4, 2022

Published online: November 27, 2022

- [1] G. J. Snyder, E. S. Toberer, *Nat. Mater.* **2008**, 7, 105.
- [2] X.-L. Shi, J. Zou, Z.-G. Chen, *Chem. Rev.* **2020**, 120, 7399.
- [3] G. Tan, L. D. Zhao, M. G. Kanatzidis, *Chem. Rev.* **2016**, 116, 12123.
- [4] Z. Liu, W. Gao, F. Guo, W. Cai, Q. Zhang, J. Sui, *Mater. Lab* **2022**, 1, 220003.
- [5] G. J. Snyder, A. H. Snyder, M. Wood, R. Gurunathan, B. H. Snyder, C. Niu, *Adv. Mater.* **2020**, 32, 2001537.
- [6] T. Zhu, Y. Liu, C. Fu, J. P. Heremans, G. J. Snyder, X. Zhao, *Adv. Mater.* **2017**, 29, 1605884.
- [7] Y. Pei, X. Shi, A. LaLonde, H. Wang, L. Chen, G. J. Snyder, *Nature* **2011**, 473, 66.
- [8] J. P. Heremans, V. Jovovic, E. S. Toberer, A. Saramat, K. Kurosaki, A. Charoenphakdee, S. Yamanaka, G. J. Snyder, *Science* **2008**, 321, 554.
- [9] C. Gayner, Y. Amouyal, *Adv. Funct. Mater.* **2019**, 30, 1901789.
- [10] B. Jiang, W. Wang, S. Liu, Y. Wang, C. Wang, Y. Chen, L. Xie, M. Huang, J. He, *Science* **2022**, 377, 208.
- [11] K. Biswas, J. He, I. D. Blum, C. I. Wu, T. P. Hogan, D. N. Seidman, V. P. Dravid, M. G. Kanatzidis, *Nature* **2012**, 489, 414.
- [12] B. Poudel, Q. Hao, Y. Ma, Y. Lan, A. Minnich, B. Yu, X. Yan, D. Wang, A. Muto, D. Vashaee, X. Chen, J. Liu, M. S. Dresselhaus, G. Chen, Z. Ren, *Science* **2008**, 320, 634.
- [13] T. Luo, J. J. Kuo, K. J. Griffith, K. Imasato, O. Cojocaru-Mirédin, M. Wuttig, B. Gault, Y. Yu, G. J. Snyder, *Adv. Funct. Mater.* **2021**, 31, 2100258.
- [14] T. Luo, F. Serrano-Sánchez, H. Bishara, S. Zhang, B. Villoro, J. J. Kuo, C. Felser, C. Scheu, G. J. Snyder, J. P. Best, G. Dehm, Y. Yu, D. Raabe, C. Fu, B. Gault, *Acta Mater.* **2021**, 217, 117147.
- [15] D. Raabe, M. Herbig, S. Sandlöbes, Y. Li, D. Tytko, M. Kuzmina, D. Ponge, P. P. Choi, *Curr. Opin. Solid State Mater. Sci.* **2014**, 18, 253.
- [16] F. Zhang, D. Wu, J. He, *Mater. Lab* **2022**, 1, 220012.
- [17] M. P. Seah, E. D. Hondros, *Proc. R. Soc. London, Ser. A* **1973**, 335, 191.
- [18] M. V. Speight, *Acta Metall.* **1968**, 16, 133.
- [19] H. Zhao, F. De Geuser, A. Kwiatkowski da Silva, A. Szczepaniak, B. Gault, D. Ponge, D. Raabe, *Acta Mater.* **2018**, 156, 318.
- [20] R. Kirchheim, *Acta Mater.* **2002**, 50, 413.
- [21] P. R. Cantwell, T. Frolov, T. J. Rupert, A. R. Krause, C. J. Marvel, G. S. Rohrer, J. M. Rickman, M. P. Harmer, *Annu. Rev. Mater. Res.* **2020**, 50, 465.
- [22] Y. Liu, M. Calcabrini, Y. Yu, S. Lee, C. Chang, J. David, T. Ghosh, M. C. Spadaro, C. Xie, O. Cojocaru-Mirédin, J. Arbiol, M. Ibanez, *ACS Nano* **2022**, 16, 78.
- [23] C. Zhou, Y. K. Lee, Y. Yu, S. Byun, Z. Z. Luo, H. Lee, B. Ge, Y. L. Lee, X. Chen, J. Y. Lee, O. Cojocaru-Mirédin, H. Chang, J. Im, S. P. Cho, M. Wuttig, V. P. Dravid, M. G. Kanatzidis, I. Chung, *Nat. Mater.* **2021**, 20, 1378.
- [24] B. J. Kooi, M. Wuttig, *Adv. Mater.* **2020**, 32, 1908302.
- [25] L. Guarneri, S. Jakobs, A. von Hoegen, S. Maier, M. Xu, M. Zhu, S. Wahl, C. Teichrib, Y. Zhou, O. Cojocaru-Mirédin, M. Raghuwanshi, C. F. Schon, M. Drogeler, C. Stampfer, R. Lobo, A. Piarristeguy, A. Pradel, J. Y. Raty, M. Wuttig, *Adv. Mater.* **2021**, 33, 2102356.
- [26] M. Wuttig, V. L. Deringer, X. Gonze, C. Bichara, J. Y. Raty, *Adv. Mater.* **2018**, 30, 1803777.
- [27] M. Zhu, O. Cojocaru-Mirédin, A. M. Mio, J. Keutgen, M. Kupers, Y. Yu, J. Y. Cho, R. Dronskowski, M. Wuttig, *Adv. Mater.* **2018**, 30, 1706735.
- [28] J. Y. Raty, M. Schumacher, P. Golub, V. L. Deringer, C. Gatti, M. Wuttig, *Adv. Mater.* **2019**, 31, 1806280.
- [29] J.-Y. Raty, M. Wuttig, *J. Phys. D: Appl. Phys.* **2020**, 53, 234002.
- [30] Y. Yu, M. Cagnoni, O. Cojocaru-Mirédin, M. Wuttig, *Adv. Funct. Mater.* **2020**, 30, 1904862.
- [31] X. Zhang, Z. Bu, S. Lin, Z. Chen, W. Li, Y. Pei, *Joule* **2020**, 4, 986.
- [32] M. Hong, J. Zou, Z. G. Chen, *Adv. Mater.* **2019**, 31, 1807071.
- [33] R. K. Vankayala, T. W. Lan, P. Parajuli, F. Liu, R. Rao, S. H. Yu, T. L. Hung, C. H. Lee, S. I. Yano, C. R. Hsing, D. L. Nguyen, C. L. Chen, S. Bhattacharya, K. H. Chen, M. N. Ou, O. Rancu, A. M. Rao, Y. Y. Chen, *Adv. Sci.* **2020**, 7, 2002494.
- [34] S. Perumal, S. Roychowdhury, D. S. Negi, R. Datta, K. Biswas, *Chem. Mater.* **2015**, 27, 7171.
- [35] M. Hong, W. Lyv, M. Li, S. Xu, Q. Sun, J. Zou, Z.-G. Chen, *Joule* **2020**, 4, 2030.
- [36] M. Hong, K. Zheng, W. Lyv, M. Li, X. Qu, Q. Sun, S. Xu, J. Zou, Z.-G. Chen, *Energy Environ. Sci.* **2020**, 13, 1856.
- [37] D. Wu, L. D. Zhao, S. Hao, Q. Jiang, F. Zheng, J. W. Doak, H. Wu, H. Chi, Y. Gelbstein, C. Uher, C. Wolverton, M. Kanatzidis, J. He, *J. Am. Chem. Soc.* **2014**, 136, 11412.
- [38] J. Li, X. Zhang, Z. Chen, S. Lin, W. Li, J. Shen, I. T. Witting, A. Faghaninia, Y. Chen, A. Jain, L. Chen, G. J. Snyder, Y. Pei, *Joule* **2018**, 2, 976.
- [39] Z. Liu, W. Gao, W. Zhang, N. Sato, Q. Guo, T. Mori, *Adv. Energy Mater.* **2020**, 10, 2002588.
- [40] J. Li, X. Zhang, X. Wang, Z. Bu, L. Zheng, B. Zhou, F. Xiong, Y. Chen, Y. Pei, *J. Am. Chem. Soc.* **2018**, 140, 16190.
- [41] X. Zhang, J. Li, X. Wang, Z. Chen, J. Mao, Y. Chen, Y. Pei, *J. Am. Chem. Soc.* **2018**, 140, 15883.
- [42] Z. Zheng, X. Su, R. Deng, C. Stoumpos, H. Xie, W. Liu, Y. Yan, S. Hao, C. Uher, C. Wolverton, M. G. Kanatzidis, X. Tang, *J. Am. Chem. Soc.* **2018**, 140, 2673.
- [43] Z. Liu, J. Sun, J. Mao, H. Zhu, W. Ren, J. Zhou, Z. Wang, D. J. Singh, J. Sui, C. W. Chu, Z. Ren, *Proc. Natl. Acad. Sci. USA* **2018**, 115, 5332.
- [44] G. Bai, Y. Yu, X. Wu, J. Li, Y. Xie, L. Hu, F. Liu, M. Wuttig, O. Cojocaru-Mirédin, C. Zhang, *Adv. Energy Mater.* **2021**, 11, 2102012.
- [45] B. Srinivasan, A. Gellé, F. Gucci, C. Boussard-Plédel, B. Fontaine, R. Gautier, J.-F. Halet, M. J. Reece, B. Bureau, *Inorg. Chem. Front.* **2019**, 6, 63.
- [46] H.-S. Nam, D. J. Srolovitz, *Phys. Rev. Lett.* **2007**, 99, 025501.
- [47] T. Xing, Q. Song, P. Qiu, Q. Zhang, X. Xia, J. Liao, R. Liu, H. Huang, J. Yang, S. Bai, D. Ren, X. Shi, L. Chen, *Natl. Sci. Rev.* **2019**, 6, 944.
- [48] M. Hong, Y. Wang, T. Feng, Q. Sun, S. Xu, S. Matsumura, S. T. Pantelides, J. Zou, Z. G. Chen, *J. Am. Chem. Soc.* **2019**, 141, 1742.
- [49] M. Hong, W. Lyu, Y. Wang, J. Zou, Z. G. Chen, *J. Am. Chem. Soc.* **2020**, 142, 2672.
- [50] M. Sist, H. Kasai, E. M. J. Hedegaard, B. B. Iversen, *Phys. Rev. B* **2018**, 97, 094116.
- [51] A. Edwards, A. Pineda, P. Schultz, M. Martin, A. Thompson, H. Hjalmarson, C. Umrigar, *Phys. Rev. B* **2006**, 73, 045210.
- [52] P. Jood, J. P. Male, S. Anand, Y. Matsushita, Y. Takagiwa, M. G. Kanatzidis, G. J. Snyder, M. Ohta, *J. Am. Chem. Soc.* **2020**, 142, 15464.
- [53] P. R. Cantwell, M. Tang, S. J. Dillon, J. Luo, G. S. Rohrer, M. P. Harmer, *Acta Mater.* **2014**, 62, 1.
- [54] H.-S. Kim, Z. M. Gibbs, Y. Tang, H. Wang, G. J. Snyder, *APL Mater.* **2015**, 3, 041506.
- [55] Y. Feng, J. Li, Y. Li, T. Ding, C. Zhang, L. Hu, F. Liu, W. Ao, C. Zhang, *J. Mater. Chem. A* **2020**, 8, 11370.
- [56] P. Li, T. Ding, J. Li, C. Zhang, Y. Dou, Y. Li, L. Hu, F. Liu, C. Zhang, *Adv. Funct. Mater.* **2020**, 30, 1910059.

- [57] M. Wuttig, D. Lusebrink, D. Wamwangi, W. Welnic, M. Gillessen, R. Dronskowski, *Nat. Mater.* **2007**, 6, 122.
- [58] M. Hong, Z. G. Chen, *Acc. Chem. Res.* **2022**, 55, 3178.
- [59] Q. Sun, M. Li, X.-L. Shi, S.-D. Xu, W.-D. Liu, M. Hong, W.-y. Lyu, Y. Yin, M. Dargusch, J. Zou, Z.-G. Chen, *Adv. Energy Mater.* **2021**, 11, 2100544.
- [60] T. Xing, C. Zhu, Q. Song, H. Huang, J. Xiao, D. Ren, M. Shi, P. Qiu, X. Shi, F. Xu, L. Chen, *Adv. Mater.* **2021**, 33, 2008773.
- [61] J. Dong, F.-H. Sun, H. Tang, J. Pei, H.-L. Zhuang, H.-H. Hu, B.-P. Zhang, Y. Pan, J.-F. Li, *Energy Environ. Sci.* **2019**, 12, 1396.
- [62] Y. Gelbstein, J. Davidow, S. N. Girard, D. Y. Chung, M. Kanatzidis, *Adv. Energy Mater.* **2013**, 3, 815.
- [63] S. Perumal, M. Samanta, T. Ghosh, U. S. Shenoy, A. K. Bohra, S. Bhattacharya, A. Singh, U. V. Waghmare, K. Biswas, *Joule* **2019**, 3, 2565.
- [64] Z. Bu, X. Zhang, B. Shan, J. Tang, H. Liu, Z. Chen, S. Lin, W. Li, Y. Pei, *Sci. Adv.* **2021**, 7, eabf2738.
- [65] Y. Yu, X. Xu, Y. Wang, B. Jia, S. Huang, X. Qiang, B. Zhu, P. Lin, B. Jiang, S. Liu, X. Qi, K. Pan, D. Wu, H. Lu, M. Bosman, S. J. Pennycook, L. Xie, J. He, *Nat. Commun.* **2022**, 13, 5612.
- [66] Y. Liu, X. Zhang, P. Nan, B. Zou, Q. Zhang, Y. Hou, S. Li, Y. Gong, Q. Liu, B. Ge, O. Cojocaru-Mirédin, Y. Yu, Y. Zhang, G. Chen, M. Wuttig, G. Tang, *Adv. Funct. Mater.* **2022**, 32, 2209980.
- [67] Y. Yu, C. Zhou, S. Zhang, M. Zhu, M. Wuttig, C. Scheu, D. Raabe, G. J. Snyder, B. Gault, O. Cojocaru-Mirédin, *Mater. Today* **2020**, 32, 260.
- [68] B. Gault, A. Chiamonti, O. Cojocaru-Mirédin, P. Stender, R. Dubosq, C. Freysoldt, S. K. Makineni, T. Li, M. Moody, J. M. Cairney, *Nat. Rev. Methods Primers* **2021**, 1, 51.
- [69] Y. Yu, C. Zhou, X. Zhang, L. Abdellaoui, C. Doberstein, B. Berkels, B. Ge, G. Qiao, C. Scheu, M. Wuttig, O. Cojocaru-Mirédin, S. Zhang, *Nano Energy* **2022**, 101, 107576.
- [70] C. Rodenkirchen, M. Cagnoni, S. Jakobs, Y. Cheng, J. Keutgen, Y. Yu, M. Wuttig, O. Cojocaru-Mirédin, *Adv. Funct. Mater.* **2020**, 30, 1910039.
- [71] T. Chookajorn, A. M. Heather, A. Schuh Christopher, *Science* **2012**, 337, 951.
- [72] D. An, J. Wang, J. Zhang, X. Zhai, Z. Kang, W. Fan, J. Yan, Y. Liu, L. Lu, C.-L. Jia, M. Wuttig, O. Cojocaru-Mirédin, S. Chen, W. Wang, G. J. Snyder, Y. Yu, *Energy Environ. Sci.* **2021**, 14, 5469.
- [73] B. Färber, E. Cadel, A. Menand, G. Schmitz, R. Kirchheim, *Acta Mater.* **2000**, 48, 789.
- [74] L. Wu, X. Li, S. Wang, T. Zhang, J. Yang, W. Zhang, L. Chen, J. Yang, *NPGA. Mater.* **2017**, 9, e343.
- [75] J. J. Kuo, S. D. Kang, K. Imasato, H. Tamaki, S. Ohno, T. Kanno, G. J. Snyder, *Energy Environ. Sci.* **2018**, 11, 429.
- [76] Y. Lin, M. Wood, K. Imasato, J. J. Kuo, D. Lam, A. N. Mortazavi, T. J. Slade, S. A. Hodge, K. Xi, M. G. Kanatzidis, D. R. Clarke, M. C. Hersam, G. J. Snyder, *Energy Environ. Sci.* **2020**, 13, 4114.
- [77] S. Roychowdhury, T. Ghosh, R. Arora, M. Samanta, L. Xie, N. K. Singh, A. Soni, J. He, U. V. Waghmare, K. Biswas, *Science* **2021**, 371, 722.
- [78] R. Chetty, Y. Kikuchi, Y. Bouyrie, P. Jood, A. Yamamoto, K. Suekuni, M. Ohta, *J. Mater. Chem. C* **2019**, 7, 5184.
- [79] Z. Bu, X. Zhang, Y. Hu, Z. Chen, S. Lin, W. Li, Y. Pei, *Energy Environ. Sci.* **2021**, 14, 6506.
- [80] T. Xing, Q. Song, P. Qiu, Q. Zhang, M. Gu, X. Xia, J. Liao, X. Shi, L. Chen, *Energy Environ. Sci.* **2021**, 14, 995.
- [81] B. Jia, Y. Huang, Y. Wang, Y. Zhou, X. Zhao, S. Ning, X. Xu, P. Lin, Z. Chen, B. Jiang, J. He, *Energy Environ. Sci.* **2022**, 15, 1920.
- [82] J. Chu, J. Huang, R. Liu, J. Liao, X. Xia, Q. Zhang, C. Wang, M. Gu, S. Bai, X. Shi, L. Chen, *Nat. Commun.* **2020**, 11, 2723.
- [83] P. Qiu, T. Mao, Z. Huang, X. Xia, J. Liao, M. T. Agne, M. Gu, Q. Zhang, D. Ren, S. Bai, X. Shi, G. J. Snyder, L. Chen, *Joule* **2019**, 3, 1538.
- [84] Y. Xing, R. Liu, J. Liao, Q. Zhang, X. Xia, C. Wang, H. Huang, J. Chu, M. Gu, T. Zhu, C. Zhu, F. Xu, D. Yao, Y. Zeng, S. Bai, C. Uher, L. Chen, *Energy Environ. Sci.* **2019**, 12, 3390.
- [85] G. Kresse, J. Furthmüller, *Phys. Rev. B* **1996**, 54, 11169.
- [86] J. P. Perdew, K. Burke, M. Ernzerhof, *Phys. Rev. Lett.* **1996**, 77, 3865.
- [87] G. Kresse, D. Joubert, *Phys. Rev. B* **1999**, 59, 1758.
- [88] H. J. Monkhorst, J. D. Pack, *Phys. Rev. B* **1976**, 13, 5188.
- [89] V. Wang, N. Xu, J.-C. Liu, G. Tang, W.-T. Geng, *Comput. Phys. Commun.* **2021**, 267, 108033.